AD-A140 878 EVALUATION OF STOKES SETTLING EQUATION FOR VARIABLE DENSITY AGGREGATES(U) UNIVERSITY OF SOUTH FLORIDA ST PETERSBURG DEPT OF MARINE SCIENCE K L CARDER ET AL. 1/1

UNCLASSIFIED 26 APR 84 N00014-83-K-0082 F/G 8/8 NL

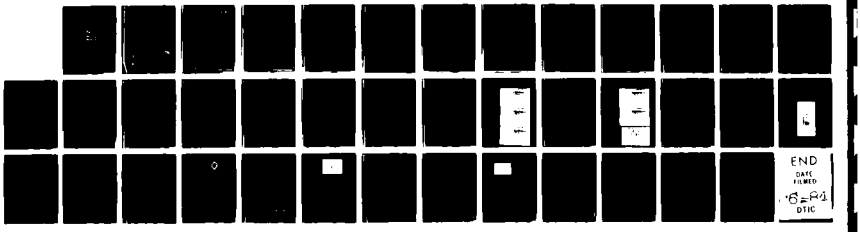

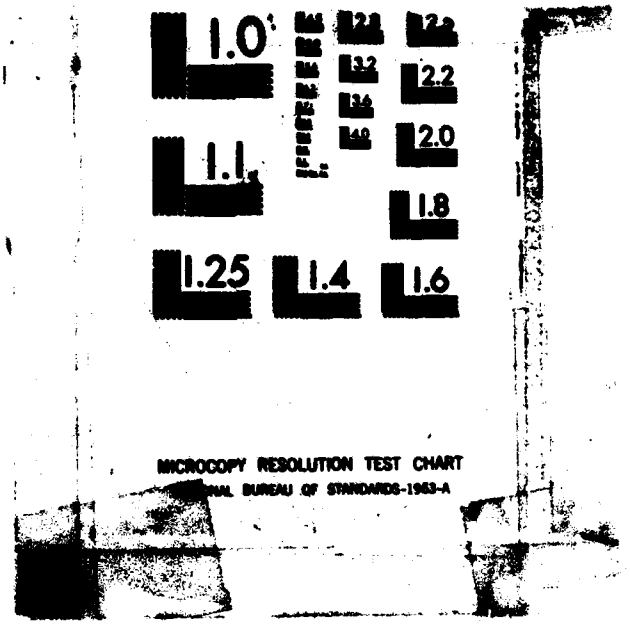
1.0
1.1
1.25
1.4
1.6
2.2
2.0
1.8
MICROCOPY RESOLUTION TEST CHART
NAL BUREAU OF STANDARDS-1963-A

FINAL REPORT
for
Office of Naval Research

Contract No. N00014-83-K-0082

Evaluation of Stokes Settling Equation for Variable Density Aggregates

by

Kendall L. Carder
and
Robert G. Steward

Department of Marine Science
University of South Florida
140 Seventh Avenue South
St. Petersburg, Florida 33701

SECURITY CLASSIFICATION OF THIS PAGE (When Data Entered)

REPORT DOCUMENTATION PAGE

READ INSTRUCTIONS BEFORE COMPLETING FORM

1. REPORT NUMBER	2. GOVT ACCESSION NO. AD-A140 878
3. RECIPIENT'S CATALOG NUMBER	
4. TITLE (and Subtitle) Stokes Settling Equation for Variable Density Aggregates	5. TYPE OF REPORT & PERIOD COVERED Final Technical Report 11-1-82 to 2-29-84
	6. PERFORMING ORG. REPORT NUMBER
7. AUTHOR(s) Kendall L. Carder Robert G. Steward	8. CONTRACT OR GRANT NUMBER(s) N00014-83-K-0082
9. PERFORMING ORGANIZATION NAME AND ADDRESS Department of Marine Science University of South Florida, 140 Seventh Ave. S. St. Petersburg, Florida 33701	10. PROGRAM ELEMENT, PROJECT, TASK AREA & WORK UNIT NUMBERS N00014-83-K-0082
11. CONTROLLING OFFICE NAME AND ADDRESS Office of Naval Research Ocean Science and Technology Division Code 480,482 NSTL Station, MS 39529	12. REPORT DATE April 26, 1984
	13. NUMBER OF PAGES
14. MONITORING AGENCY NAME & ADDRESS (if different from Controlling Office)	15. SECURITY CLASS. (of this report) unclassified
	15a. DECLASSIFICATION/DOWNGRADING SCHEDULE

16. DISTRIBUTION STATEMENT (of this Report)
Approved for public release, distribution unlimited.

17. DISTRIBUTION STATEMENT (of the abstract entered in Block 20, if different from Report)

18. SUPPLEMENTARY NOTES
Includes reprints from J. Sed. Petr. 53(2): 643-648 and Applied Optics 23: 204-210.

19. KEY WORDS (Continue on reverse side if necessary and identify by block number)
Stokes particle settling, density, viscosity, size, shape, aggregate pore-water flushing rates, refractive index, density gradients, holography.

20. ABSTRACT (Continue on reverse side if necessary and identify by block number)

Holographic measurements of clay aggregates settling through a density/viscosity gradient revealed that the aggregate pore waters are flushed, affecting the aggregate density and settling speed. The flushed pore waters provide a low viscosity conduit in which subsequent particles settle as much as 25% faster than they would in the surrounding fluid. This effect is holographically recorded due to its reduced refractive index relative to the surrounding medium. Regions where this phenomenon may play an

DD FORM 1 JAN 73 1473 EDITION OF 1 NOV 65 IS OBSOLETE S/N 0102-014-6601

SECURITY CLASSIFICATION OF THIS PAGE

20. role are at river mouths and in shelf/slope density-gradient environments for clay aggregates, and in sea-ice-melt regions and in the microstructure of the thermoclines for low-density biogenous particles.

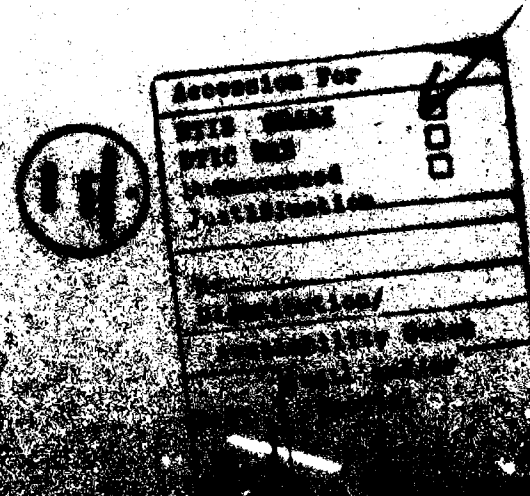

Abstract

Holographic measurements of clay aggregates settling through a density/viscosity gradient revealed that the aggregate pore waters are flushed, affecting the aggregate density and settling speed. The flushed pore waters provide a low viscosity conduit in which subsequent particles settle as much as 25% faster than they would in the surrounding fluid. This conduit is holographically recorded due to its reduced refractive index relative to the surrounding medium. Regions where this phenomenon may play an important role are at river mouths and in shelf/slope density-gradient environments for clay aggregates, and in sea-ice-melt regions and in the microstructure of the thermoclines for low-density biogenous particles.

Table of Contents

I. Introduction

Reduction of viscous drag has been cited as a reason for the relatively faster settling speeds than expected for aggregates using Stokes settling equation with a particle packing model density (Chase, 1979; Hawley, 1982). However, the inability to measure the actual density of individual particles in these studies has made it necessary to make gross estimates of one or more of the Stokesian parameters, usually the aggregate density. If settling aggregates were assigned too small a density based upon a given density packing model, it would appear that viscous reduction had occurred in order to provide faster-than-Stokes settling speeds. Also, if aggregates settled and then broke up at depth, the smaller aggregate components observed would appear to have settled faster than Stokes equation allows. Again, viscous reduction could erroneously be used to explain this settling behavior. Our program objectives were to conduct settling-chamber/density-gradient experiments to measure aggregate particle density and viscous drag independently.

A key element of the project was the independent measurement of particle density by the use of high density fluids (isotonic with the seawater) in density gradient columns. Although the holographically-measured settling velocity and Stokes equation predicted montmorillonite aggregate densities of the order 1.05 g/ml (similar to the high-order aggregates found by Krone (1976)), none of the aggregates remained buoyant in the columns of high-density sugar solutions, which reached densities of 1.40 g/ml. This suggested that the occluded water or pore water of the aggregate was

flushed and replaced by the density of the surrounding media. This would remove the buoyancy due to lower density occluded waters of the original aggregate, and the settling aggregate would have a net negative buoyancy due to the clay (montmorillonite) component. Holographic investigation of the behavior of the aggregates as they traversed a sharp density interface has demonstrated some aspects of aggregate settling behavior which are of more importance than the objectives of the initial program. Pore water flushing has been demonstrated holographically to occur and to have significant effects on the settling behavior of aggregate particles.

As a summary of the work performed under this contract, this report will describe the behavior of inorganic aggregates encountering fluids of differing composition than those in which they were created. Holographic techniques have been used to show that the interstitial water of these aggregates is not tightly bound. In fact, it is exchanged rapidly, and suggests an initiation mechanism for the formation of vertical salt fingers in stratified water columns.

II. Experimental Design

The settling chamber was constructed for this project with the following features: an upper cylinder to dampen injection forces and allow the settling particles to achieve terminal settling velocity, and a lower chamber equipped with dual ports for holographic velocimeters crossed at 90° to each other and the settling direction. Below the horizontal laser ports, the particles come to rest on another optical plane providing an opportunity to holographically image the particles in the vertical direction.

Three types of aggregates were prepared in filtered, abiotic artificial seawater. Three standard clays, kaolinite, montmorillonite, and illite from the U. S. Geological Survey were each allowed to aggregate in 35ppt artificial seawater for about one month. Flocculated aggregates on the order of 20-300 μm were gently withdrawn and introduced both to the settling chamber and the density gradient chamber.

Two different density media were used in the gradients. In the initial setup runs and test, serum dextran was used to save the extremely expensive metrizamide for later runs. Metrizamide-heavy water solutions isotonic with 35ppt seawater were created with densities as high as 1.40 g/ml. Even at these high densities, the aggregates consistently failed to become buoyant, even those with densities determined using Stokes settling equation (with measured water viscosity) to be less than 1.05 g/ml.

III. Results

To examine the behavior of the aggregates as they settled into the higher density fluids, the holographic microvelocimeter was employed. A two-layer, isothermal, isotonic density gradient was prepared from artificial seawater (35ppt, 1.0241 g/ml, 23.5°C, 0.92 centipoise) and dextran-artificial seawater (35ppt, 23.5°C, 1.054 gm/ml, 7.45 centipoise). The 1 cm diameter laser beam crossed the settling chamber at the sharp interface. Time-sequential transmission holograms revealed why the particles were not reaching density equilibrium with the heavier medium. As the particles

encountered the interface, they slowed down. After a pause of less than a second, the larger particles punched through the interface, leaving a streamer of lower-density, extruded pore water in their wake. This streamer shows up holographically since the difference in index of refraction between the pore water streamer and medium results in interference patterns.

An example of this behavior is shown in Figure 1a-e. This was the second experiment performed with this density gradient, so the original step-like structure had broken down somewhat near the interface due to the mixing induced by the settling particles of the first experiment (some ten minutes earlier). These unreconstructed holographic images show only the diffraction fringes. An in-focus reconstruction of Figure 1b is shown in the Appendix.

The first visible particle to resume settling after hitting the interface is labelled A. This particle is .0256 microns diameter and extrudes a low viscosity conduit in its wake that influences the settling of particles B and C. In addition to channelizing the subsequent particle settling paths, this conduit also tends to affect particle morphology and settling orientation. The reduced viscosity and density in the conduit and the alignment of the particle long axes with it, permits increased settling speed by the subsequent particles. This increases the likelihood that particles will collide with slower moving particles downstream, and can result in elongate aggregates with their long axis oriented vertically (shown in Figure 2). A detailed explanation of the settling behavior and flushing rate of the particles in Figure 1 is provided in the discussion.

IV. Holography of Pore Water Streamers

The tube-like conduits of flushed aggregate pore waters contain a lower density, lower viscosity, and lower refractive index media than that surrounding the conduits. The maximum refractive index contrast is $\Delta n = .0046$: that difference between that of the upper and lower layers. The streamer left by particle A stretches to about .2 cm below the original interface (about 8 diameters of particle A). If we calculate the diameter D of a cylinder .2 cm long that contained only seawater, its diameter would be on the order of .0075 cm in order that its volume match that of the volume of particle A (.0256 cm diameter).

A light ray ($\lambda = 632.8$ nm <u>in vacuo</u>) passing through the center of a seawater cylinder ($n = 1.3396$) of .0075 cm diameter would exit 0.54 wavelengths ahead in phase of the part of that wave front that passed just outside the cylinder. Since the index of refraction contrast is so small, very little refraction will occur ($n_{sw}/n_d - 1 \ll 1$). Rays passing just outside the cylinder diffract toward the central axis, where interference occurs with those having traversed through it. For a cylinder such that

$$\gamma_c = \left| \frac{k_0 D}{4} \left(\frac{n_{sw}}{n_d} - 1 \right) \right| \approx 3.9 ,$$

the [illegible] constructive interference peak [illegible] $k_0 = 2\pi/\lambda$, D is the diameter of the cylinder, [illegible] and n_d are the [illegible]

interference peak (bright fringes) which is very close to the maximum value possible. For larger cylinders with similar refractive indices, the axial interference peaks decrease, but never by more than 50%. For cylinders with $d < .0025$ cm, the amplitude of the interference peak decreases rapidly toward background values. Small destructive interference fringes (dark fringes) will occur at an angle of about 0.5° off axis and downstream from the cylinders and will be most apparent for cylinders about twice (or increments thereof) the diameter of our model cylinder ($\rho \triangleq 7, 14, 20, \ldots$).

In summary, maximum fringe formation will occur on our film if $\rho_c \triangleq 3.9$. For lower refractive index contrast (smaller $|\, n_{sw}/n_d - 1\,|$), a larger cylinder (presumably created by a larger aggregate) is required to produce similar constructive fringes. For fresh water over salt water (e.g., $m = n_{fw}/n_{sw} \triangleq \frac{1.3330}{1.3390}$), the maximum refractive contrast approaches that of our model cylinder. Only iceberg melt or river plumes over deep water scenarios (e.g., Amazon, Magdalena) might provide that much refractive contrast. However, less contrast from larger diameter cylinders (larger particles) would produce similar fringes to the ones we have viewed.

V. Particle Dynamics Model for Aggregates with Occluded Water Flushing

To understand the dynamics of porous aggregates which exchange their occluded waters at some unknown rate with that of the surrounding medium, we developed a model to estimate the density of the occluded waters as a function of a flushing factor. To begin, we require some definitions.

A wet primary particle is defined as a particle containing no voids but has water bound in the molecular matrix. The density of such a particle, ρ_p, is defined as

$$1) \quad \rho_p = \frac{M_s + M_w}{V_s + V_w}$$

where M_s and M_w are the masses of the solid material and water respectively, and V_s and V_w are volumes of the same respective materials. We have determined in previous work that the density of our samples of wet, primary montmorillonite particles is 1.77 gm/ml (Gartner and Carder, 1977).

As the material aggregates, internal voids are created, partially enclosing occluded water (ow). If this ow is tightly bound, a static density results as defined by

$$2) \quad \rho_{static} = \frac{M_s + M_w + M_{ow}}{V_s + V_w + V_{ow}} .$$

If the ow is exchanged with the surrounding medium, then a dynamic density ($\rho_{dynamic}$) results as

$$3) \quad \rho_{dynamic} = \frac{M_s + M_w + M_{ow}'}{V_s + V_w + V_{ow}} .$$

M_{ow}' is an apparent mass of ow as defined by the Stokes equation for a sphere of diameter D settling with velocity v_s in a medium of density ρ_m and viscosity η. If aggregates or phytoplankton contain the occluded water (or cytoplasm) tightly enough that there is no significant flushing or exchange of pore waters with the surrounding isotonic medium, then it follows that

4) $$\rho_{static} = \rho_{dynamic}.$$

Otherwise

$$\rho_{static} \leq \rho_{dynamic}.$$

We can describe, to the first order, the effect of the flushing of aggregate pore waters on the Stokes settling speed by developing a relationship to describe ρ_{ow}, in terms of a flushing rate for the particle. Suppose that some fraction f of the ow is flushed each time the particle settles a distance of one diameter D. Then $f/D = F$ is the flushing rate per unit distance settled. If $\rho_{ow}(Z)$ and $\rho_{ow}(Z + \Delta Z)$ are the occluded water density values at depths Z and $Z + \Delta Z$, and the density of medium ρ_m increases linearly with depth then

5) $$\rho_m(Z) = \rho_m(0) + KZ,$$

where K is a constant that describes the change in ρ with depth.

A first order approximation of the change in ρ_{ow} in settling over a short depth $\Delta Z = D$ can be expressed as

$$\frac{\Delta\rho_{ow}(Z)}{\Delta Z} \triangleq \frac{\rho_{ow}(Z + \Delta Z) - \rho_{ow}(Z)}{\Delta Z}$$

$$\triangleq \frac{f\rho_m(Z + D) + (1 - f)\rho_{ow}(Z) - \rho_{ow}(Z)}{D}$$

$$6) \qquad = \frac{f[\rho_m(0) + K(Z + D)] - f\rho_{ow}(Z)}{D},$$

where the fraction f of $\rho_{ow}(Z)$ that is flushed is replaced by the denser water of the medium $\rho_m(Z + D)$ found at depth $Z + D$. Rearranging terms, we can write the quation as a differential equation

$$\rho_{ow}'(Z) + \frac{f}{D}\rho_{ow}(Z) = \frac{f}{D}KZ + \frac{f}{D}(\rho_m(0) + KD)$$

or

$$\rho_{ow}'(Z) + F\rho_{ow}(Z) = FKZ + F(\rho_m(0) + KD),$$

where $F = f/D$.

The solution to this equation is

$$7) \quad \rho_{ow}(Z) = \rho_{ow}(0)e^{-FZ} + e^{F/Z}[\rho_m(0) + K(Z + D - 1/F)]$$

$$- \rho_m(0) - K(D - 1/F).$$

To simulate our two-layer, density-gradient, particle dynamics problem, we let $\rho_{ow}(0) = \rho_m(0) = 1.024$ g/ml and the density contrast gradient, $K \doteq .12$ g/cm^4.

We chose to exercise F over a range of values in order to evaluate the effect that the density contrast of the occluded waters with the media has on the particle settling speed for various aggregate densities. As mentioned previously, the variation in viscosity across the interface had a more significant effect on settling speed than did the change in density, and in order to arrive at a solution, we originally assumed the density contrast of the aggregate ($\rho_{dynamic} - \rho_m$) to be constant with depth. We can now estimate how much in error that assumption may have been for the various particles in this study.

Now that ρ_{ow} can be estimated as a function of flushing rate F and depth, one can solve Stokes equation for viscosity as a function of depth, given the measured settling speeds of the particles.

Since the streamer from particle A (Figure 1) affected the viscosity of the cylinder in which particles B and C traveled, it is important to analyze the viscosity encountered by particle A first. It is clear even at .2 cm below the original interface (position of particle A in Figure 1a) that a gradient in refractive index between the streamer and surrounding waters remains. Thus, we chose .25 cm

below the interface as the depth at which the density, viscosity, and refractive index gradients of the medium with depth disappeared (medium of purely layer 2 type properties). Thus,

$$K = (1.054 - 1.024)/0.25 \text{ cm} = .12 \text{ g/cm}^4.$$

$$8) \quad \eta(Z,F) = \frac{900[1.77 \text{ g/ml } VF_s + (1 - VF_s)\rho_{cw}(Z,F) - \rho_m(Z)]D^2}{18\, v_s(Z)}$$

where

$$9) \quad VF_s = \frac{\rho_{\text{organic}}(Z,F) - \rho_{cw}(Z,F)}{1.77 \text{ g/ml} - \rho_{cw}(Z,F)},$$

and $\rho_{cw}(Z,F)$ and $\rho_m(Z)$ are known from equations 7 and 5, respectively, and VF_s is the volume fraction of the aggregate occupied by solid matter. To solve exactly this set of equations, $\eta(Z,F)$ should be known at some point where a velocity measurement $v_s(Z)$ is known. We do know that $\eta(Z > .25 \text{ cm})$ is about .0745 poise; however, no velocity measurements were available at that depth since it was out of our field of view. We thus assumed a relatively smooth transition between the viscosity at .25 cm below the interface and the viscosity at .175 cm, our deepest particle velocity observation.

VI. [illegible]ion of Model

The [illegible]lting viscosities associated with the velocities of each particle for four depth intervals and two F factors are shown in Figure 3, [illegible] and three point representations of F factors

of 0.5/cm and 0.2/cm, respectively. The flushing factor had little or no effect on particles A and C since montmorillonite made up larger fractions of their mass values than for particle A (62% and 15% versus 8.6%, respectively.

The dotted lines represent regions where two different settling transitions occurred: i) in Figure 1b and 1c particle A can be seen to be settling along or just adjacent to a streamer from an earlier particle, and ii) in Figure 1d and 1e, particle C seems to have moved out of the streamer tube of particles A and B. Particle A apparently encountered a relatively constant viscosity when in the proximity of the old streamer, with the viscosity sharply increasing as it moved away from the streamer remnant. Particle C also encountered fluid of relatively constant viscosity within the streamer of particle A, with an abrupt increase occurring on passage out of it. Figure 2 reflects these facts.

Particle B settled within the streamer of particle A until Figure 1d, where it seems to have edged out of the tube. In Figure 1e it appears to be slightly behind the tube. Figure 3 also corroborates this fact, since the viscosity encountered by particle B is clearly much less (within the streamer tube) than that encountered by particle A at the same position before the streamer was extruded.

An estimate of the effective viscosity increase outside versus inside a streamer is indicated by the arrow bar of .8 centipoise on Figure 3. That represents a viscosity increase of about 25%, a significant effect.

Summary

Holography of aggregates settling through density interfaces provides a direct observation of pore-water flushing due to the contrast in refractive index between the extruded pore waters and the medium. These extruded pore-water tubes provide a pathway where subsequent particles encounter reduced viscous drag and less buoyancy than would be available outside the tube. Viscosity reductions of at least 25% were observed. This means that if two particles of similar settling speeds are following each other in a streamer tube, the second will settle faster since it encounters lower viscosity. The probability of collisions, in such a system, then, changes from one with a random or Gaussian likelihood to one that favors low density, highly porous aggregates, capable of providing a reduced viscosity, funnel-type of pathway at density interfaces for subsequent particles to traverse and within which to collide. As these aggregates build in size, they increase even more the probability of subsequent collision. Figure 2 shows several elongated aggregates apparently created by particle collisions in a streamer tube.

References Cited

Chase, R. R., 1979. Settling behaviour of natural aquatic particles. Limnology and Oceanography 24(3): 417-426.

Gartner, J. and K. Carder, 1979. A method to determine specific gravity of suspended particles using an electronic particle counter. Jour. Sed. Petr. 49(2): 631-633.

Hawley, N., 1982. Settling velocity of natural aggregates. J. Geophys. Res. 87(C12): 9489-9498.

Jerlov, N. G., 1968. Optical Oceanography, Elsevier, New York, 194 p.

Krone, R. B., 1976. Engineering interest in the benthic boundary layer, in N. McCave (ed.), The Benthic Boundary Layer, Plenum, New York: 143-156.

Van de Hulst, H. C., 1957. Light Scattering by Small Spheres, Wiley, New York, 470 p.

Figures 1a (top), 1b (middle), 1c (bottom), 1d (top: next page), 1e (middle: next page). A sequence of holograms taken with 0.5 second spacing. Top arrow is where the original (before experiment) density interface was located and represents our reference (Z = 0) point. Three aggregates labeled A (246 μm diameter), B (76.5 μm diameter), and C (113.5 μm diameter) are settling along the same pathway, which is marked by a bright pore-water streamer emanating from particle A. In Figures 1d and 1e particles B and C appear to be diverted from this streamer, perhaps being influenced by the proximity of the remnant streamer on the immediate left. Note the apparent formation of an elongated aggregate in the streamer just above particle C.

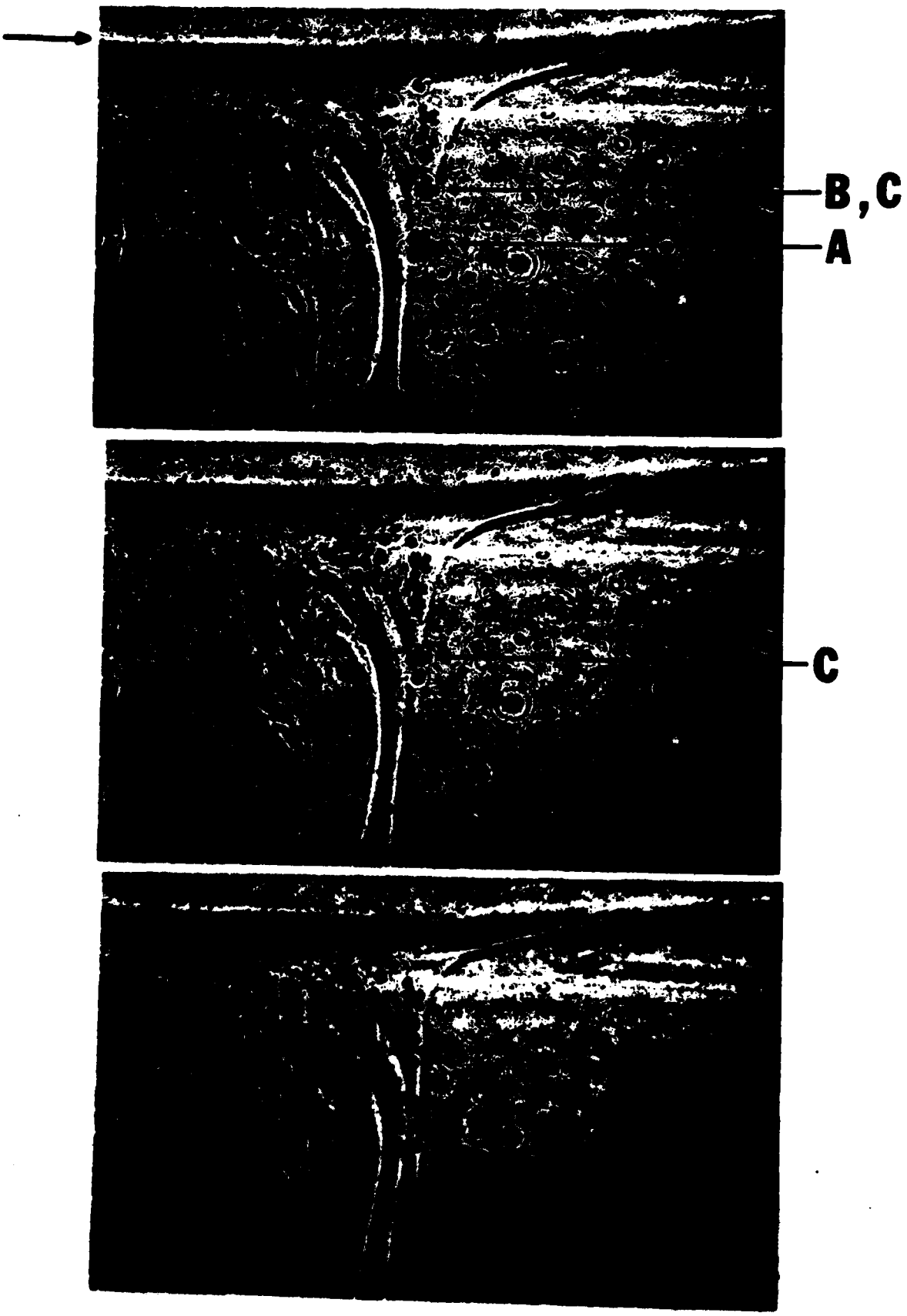
B,C
A
C

Figure 2 (bottom). Hologram of several elongated aggregates found about 1 cm below the interface (note especially the lower left corner). These streamlined morphologies suggest their formation to have occurred in a streamer. Note the continued presence of low index streamers even this far below the interface, suggesting relatively slow flushing rates.

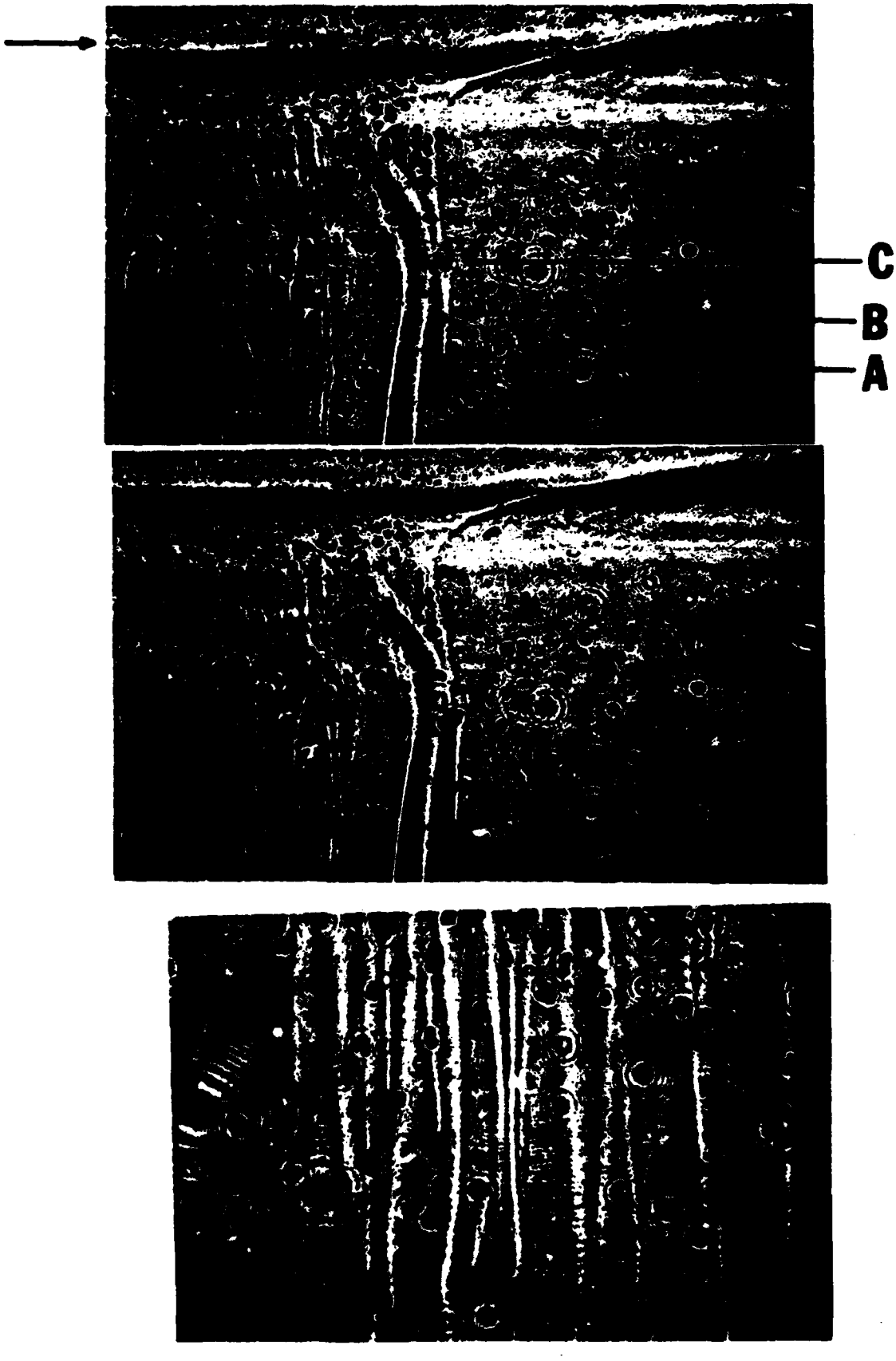
C
B
A

Figure 3. Viscosity profile in the density gradient traversed by and inferred from particles A, B, and C. The sudden increase in viscosity observed for particle C some .11 cm below the interface occurred when the particle left the low viscosity streamer and suddenly encountered more resistance to settling.

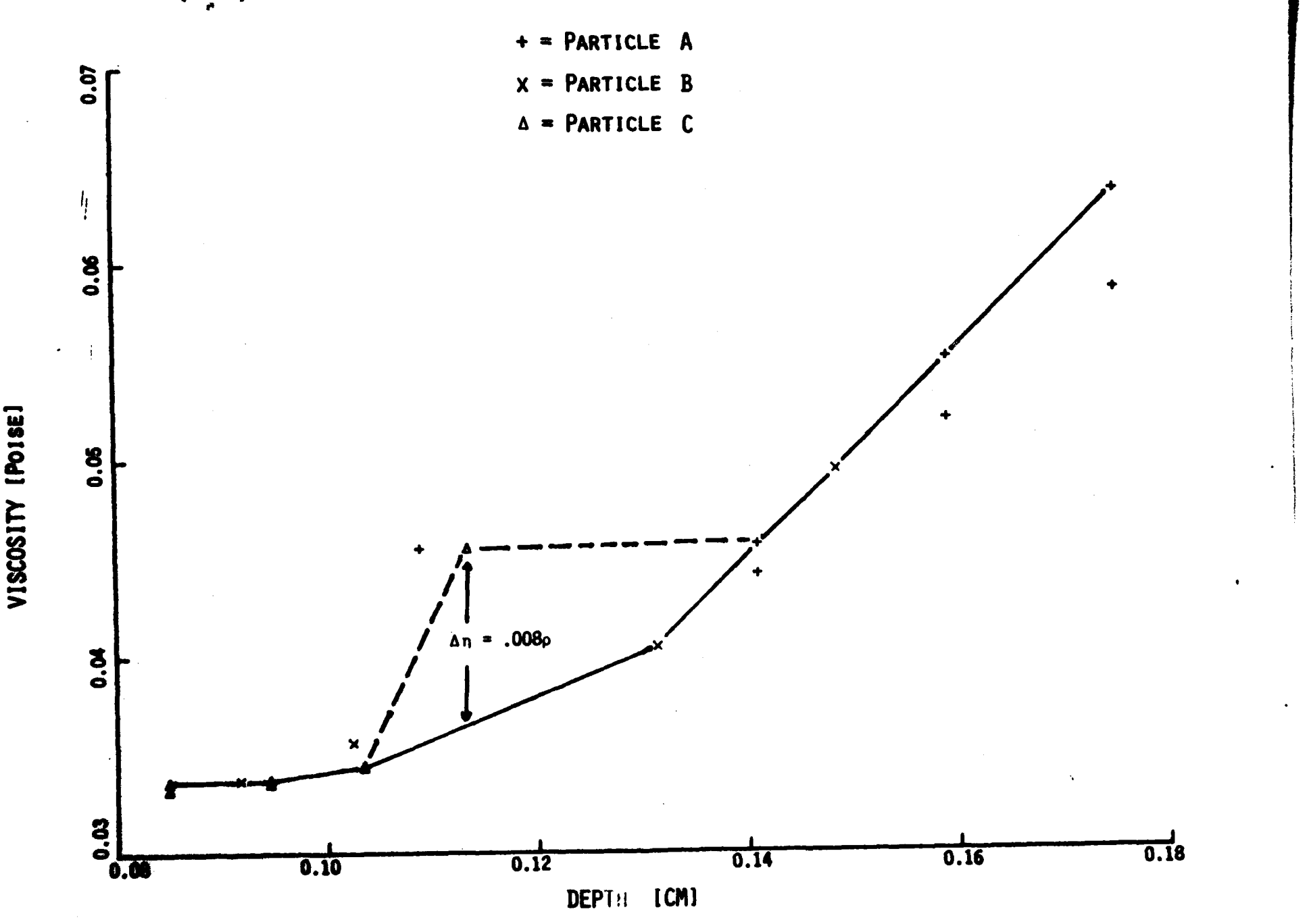
+ = PARTICLE A
X = PARTICLE B
Δ = PARTICLE C
VISCOSITY [POISE]
0.07
0.06
0.05
0.04
0.03
Δη = .008ρ
0.08
0.10
0.12
0.14
0.16
0.18
DEPTH [CM]

APPENDIX B

In-focus images of particles A, B, and C after holographic reconstruction.

Reprinted from Applied Optics, Vol. 23, page 204, January 15, 1984

Image analysis techniques for holograms of dynamic oceanic particles

Paul R. Payne, Kendall L. Carder, and Robert G. Steward

A holographic image analysis system has been developed to measure position, velocity, size, and shape of microscopic particles settling in 3-D space. Images of particles recorded sequentially on individual holographic frames are reconstructed using an in-line far-field configuration, registered in 3-D space, and particle displacements (velocities) between sequential frames are determined. Particle settling velocity is calculated using elapsed time between frames. Digitized video signals of the reconstructed holographic images are processed to determine particle size, shape, and area to facilitate identification by shape from frame to frame and to calculate particle specific gravities. A cataloging system was developed to provide efficient data management.

I. Introduction

Measurements of size, shape, and density are critical factors in the study of particle dynamics and settling characteristics of marine hydrosols. Micrographic holography has been widely used in aerosol studies[1] and holographic movie cameras have been developed for studying zooplankton feeding behavior in ocean waters.[2] Using a similar holographic technique, the size and settling behavior of aggregates resulting from mixing riverine water with seawater has been determined in the laboratory[3] and the effect of particle shape on the settling velocities of primary hydrosols (unaggregated) has also been investigated.[4,5]

Carder *et al.*[6] have developed an *in situ* holographic microvelocimeter for the study of microscopic particles suspended in seawater. This device records the image of each particle in 3-D space on a series of successive holograms with respect to time. Horizontal and vertical dimensions and cross-sectional area have been used to determine particle density using the Stokes theorem.[3] Edge coordinates are useful for particle identification (e.g., Zernike moments) and analysis of shape on particle rotation and settling speed.[4] During these studies, a great number of samples must be analyzed in order to provide sufficient statistics for determining particle population characteristics of shape and size as well as settling velocity, trajectory, orientation, and oscillations. Such measurements can be facilitated by use of a computer-controlled image analysis system to improve the accuracy and reduce the number of man-hours in analyzing holographic particle data.

II. Problem Definition

A measurement technique was needed to determine the position, size, shape, orientation, and velocity of microscopic particles moving in 3-D space. The marine particles of interest in the study[6] cited above typically ranged from 5 to 250 μm in diameter, which necessitated the use of microscopic techniques for any detailed size or shape analysis. Since oceanic particle densities may vary from ~1.03 to 5.2 g/mliter and typical settling velocities may range from <0.0001 to 1.0 cm/sec, a variety of frame or sample periods from <1 sec to as much as 1 min may be necessary in order to provide short-term velocity measurement accuracy. In addition, the duration or exposure time for the position measurement should be <1/500 sec in order to maintain sufficient positional accuracy and prevent hologram smearing. Therefore, a relatively high-speed microscopic technique was developed[6] to record the images of multiple particles as they settled in 3-D space. To deal with the enormous data volume generated in applying these techniques (more than 50 particles/hologram), an automated method for reconstructing and analyzing the particle data has been developed. Edge coordinates are recorded when needed for particle identification and for analysis of the particle shape effects on particle rotation.

Paul Payne is with Aztec Computer Engineering, 6805 Circle Creek Drive, Pinellas Park, Florida 33565; the other authors are with University of South Florida, Department of Marine Science, St. Petersburg, Florida 33701.

Received 11 August 1983.
0003-6935/84/020204-07$02.00/0.

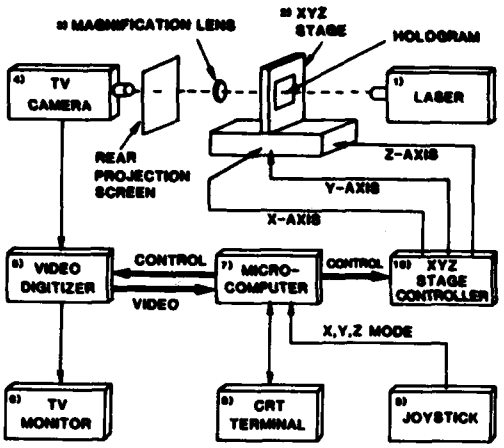

Fig. 1. Holographic image analysis system block diagram.

III. System Description

A functional block diagram of the holographic image analysis system is shown in Fig. 1. The major components and functions are: (1) a laser to reconstruct the holographic image, (2) a mechanical stage to position the hologram in 3-D space, (3) a magnification lens and rear projection screen on which to reconstruct the particle image, (4) a TV camera to produce a video signal of the image, (5) a video digitizer to convert the video signal into digital data, (6) a TV monitor to display the particle image, (7) a microcomputer with disk storage for processing and storing input data from the video digitizer and controlling the position of the mechanical stage, (8) an interactive terminal to enable operator control of the system, (9) a joystick for manual control of the frame position, and (10) the *XYZ* drive controller to move the holographic frame in the laser beam. Table I presents a list of the equipment which comprises the system.

The system is designed to perform the following functions: (1) determine the position of a particle with respect to a 3-D frame reference, (2) determine the width, height, cross-sectional area, and perimeter of a particle using a scanning algorithm, (3) determine the cross-sectional area, perimeter, and edge coordinates of the particle using a tracking algorithm, (4) enable particle identification from frame to frame by displaying the particle position and edge points (shape) from the previous holographic frame on the current frame, and (5) calculate the velocity, average diameter, and particle density from the recorded data for each particle.

Table I. Holographic Image Analysis System Equipment

Item	Description	Manufacturer	Model
1	Laser, 15-mW He–Ne	Spectra-Physics	124B
2	*XYZ* axes table	Aerotech, XY: Z:	ATS-303 ATS-416
3	28- or 50-mm lens	Nikon	
4	TV camera, high resolution	Dage	650
5	Video digitizer	Colorado video	270A
6	TV monitor	Panasonic	WV 5300
7	Microcomputer, Z-80, dual disk	Cromemco	Z-2D
8	CRT terminal	Soroc	IQ 120
9	Joystick	Cromemco	JS-1W
10	*XYZ* drive controller	Aerotech	EC-2

IV. Technical Discussion

Successive holograms of settling particles were recorded *in situ* on negative holographic transparency film using the particle velocimeter described in Ref. 6 with 4× magnification. The film was processed using standard photographic techniques and mounted on individual frames. Each holographic frame was positioned in a laser beam to reconstruct a 2-D profile of each particle in the direct transmission mode with an additional magnification of 25–40, depending on the particle size. With this particular setup we have measured particles down to 10-μm diam (see Ref. 3). Increased magnification onto the holographic film is required to measure smaller particles.

The image of each particle was successively focused on the rear projection screen by moving the holographic frame in the Z axis. The projected scene was viewed with a TV camera and converted into a digitized video signal. The holographic frame was then moved in the X and Y axes to bring the focused image of each particle into the center of the TV monitor screen. The position of the frame and the size, shape, and orientation of each particle were analyzed and recorded by the computer. As images of the same particles in subsequent frames were cataloged, a matrix of settling velocity and lateral motion characteristics was generated for each particle. The statistical distribution of settling velocity with respect to particle size, shape, and orientation provided an accurate determination of particle density and ultimately permitted a general particle classification (e.g., organic, mineral, heavy mineral), based largely on density.

A. Particle Position and Velocity

Particle settling velocity using the system described in Fig. 1 was determined by measuring the position of each particle in 3-D space at two or more different sample times. A typical particle configuration is shown in Fig. 2. Prior to cataloging any particle images from a frame, an accurate and repeatable reference is established for a point common to all frames. The reference point in a frame is centered on the TV monitor by moving the frame in the X, Y, and Z axes under computer control with a joystick. The image of each particle in the frame is then subsequently moved to the center of the monitor with the joystick and its position recorded. Size and orientation parameters are determined using the particle scanning and edge-tracking algorithms described below. Once recorded, the particle data from a previous frame can be retrieved and the *XYZ* stage driven to that position under computer control to enhance location and identification of that

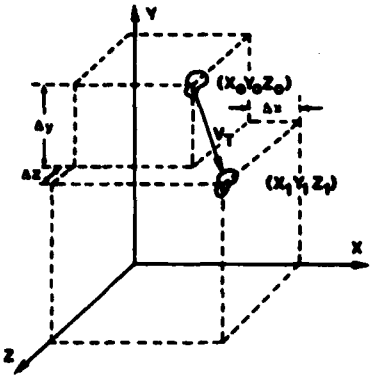

Fig. 2. Particle moving in 3-D space.

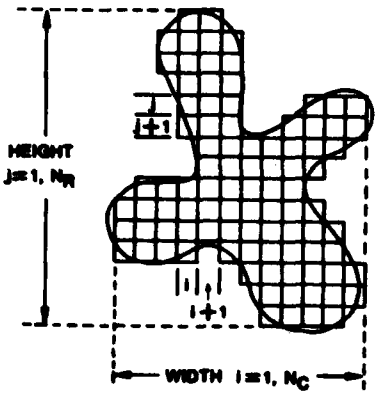

Fig. 3. Scanning algorithm processes pixels above threshold for area and perimeter.

particle on a subsequent frame. When the entry of data for all frames has been completed, the distance each particle has traveled between successive frames is determined and the individual velocities calculated.

B. Particle Area and Perimeter

Determination of the projected cross-sectional area of a particle can be derived from the reconstructed image by counting the number of pixels inside the particle boundary. In a similar manner, the perimeter of the particle can be derived from the number of pixels along the edge. One of the major problems with a noisy image is detection of the pixels which represent the edge. Yakimovsky discussed an edge detection technique[7] based on maximizing the likelihood ratio with a simple single-pass region-growing algorithm. This ratio is a comparison of the intensities of neighboring pixels within the same object to neighboring pixels within two different objects. The boundary decision is based on comparing the ratio with a predefined threshold and accumulating those neighborhoods which are considered to be within a single object into one contiguous region. McKee and Aggarwal have developed a multipass technique[8] which processes a full video frame of data to obtain edge coordinates of very complex shapes. However, this method would be far more complex and time-consuming than necessary for determination of area and perimeter in most of our applications. Also, it is rare for more than one particle image to be found in a given focal plane.

Therefore, we have chosen an image scanning technique which uses a simplified edge detection process that is based on a comparison of the pixel intensity with a threshold adjusted for the average intensity between the particle and background to determine particle area and perimeter. Pixels at each transition across the threshold are accumulated as the perimeter of the particle, while pixels above the threshold are accumulated as its area.

C. Particle Area Scan Technique

The particle scanning algorithm developed for this system is based on a simplified single-pass edge detection process. The surface area and edge perimeter of each particle are determined by comparing the video intensity of each pixel to a selected threshold value. The technique consists of processing a series of vertical scans which horizontally cover the image as depicted in Fig. 3. The horizontal (equatorial) and vertical (polar) axes of the particle are determined by manually adjusting a vertically scanning cursor to the edges of the particle when the algorithm is first executed for each measurement. This limits the region under investigation to the immediate environment of the particle and eliminates the generally out-of-focus neighboring particles from consideration.

Beginning on the left side, the particle is scanned from top to bottom in synchronism with the TV raster. The video intensity (0–255) of each pixel is compared to a threshold value corresponding to the intensity at the particle edge. If the pixel intensity is greater than the threshold, the pixel area is assigned a unit value and the column area is incremented. Otherwise, its value is zero. If the pixel area value is different from that of the last pixel, the horizontal perimeter is incremented. When the vertical scan is complete, the difference between areas of current and previous columns is added to the vertical perimeter. The scan is then incremented to the right and the process repeated until the entire particle has been scanned. The selected scan consists of N_r rows vertically and N_c columns horizontally. The total area of the particle is the sum of all column areas scaled as shown in Eq. (1). Since the shape of each pixel is not square, the vertical component must be scaled to provide an accurate measurement of the area and perimeter. Or simply,

$$\text{if } V_{p(i,j)} > V_t \text{ then } A_{p(i,j)} = 1,$$

$$\text{if } V_{p(i,j)} < V_t \text{ then } A_{p(i,j)} = 0,$$

$$\text{Area} = F_x \cdot F_y \cdot \sum_{i=1}^{N_c} \left[\sum_{j=1}^{N_r} A_{p(i,j)} \right], \quad (1)$$

where i and j are the pixel column and row,
V_p is the video amplitude of pixel (i,j),
V_t is the preselected video threshold,
N_c is the number of scanned columns,
N_r is the number of scanned rows,
F_x is the horizontal scale factor, and
F_y is the vertical scale factor.

The error introduced by the quantization of area should converge toward zero and become negligible as the size of the particle increases.

The vertical component of the perimeter (P_v) is the difference between the number of pixels above the threshold in one column compared with the number in the previous column. The horizontal component (P_h) is the sum of all transitions across the threshold occurring in each column. The horizontal and vertical components are scaled by F_x and F_y, respectively, and combined to form the particle perimeter as shown in Eq. (2). If $V_p(i,j)$ is not equal to $V_p(i,j+1)$, the incremental horizontal component $H_p(i,j) = 1$, otherwise $H_p(i,j) = 0$:

$$\text{perimeter} = (F_x \cdot P_h) + (F_y \cdot P_v), \tag{2}$$

where

$$P_h = \sum_{i=1}^{N_c} \left[\sum_{j=1}^{N_r} H_p(i,j) \right],$$

$$P_v = \sum_{i=1}^{N_c} \left[\sum_{j=1}^{N_r} A_p(i,j) - \sum_{j=1}^{N_r} A_p(i-1,j) \right].$$

The major error in this method is highly dependent on the orientation of any edge segment with respect to the scanning axis. Although straight edges orthogonal to the scan will yield good measurements of perimeter, those same straight edges oriented diagonally to the scan axis can degrade the perimeter measurement by as much as 30% [1-SQRT (1/2)]. Therefore, a different method of determining perimeter which will be insensitive to particle orientation was required. Also, variations in the pixel intensity around the particle perimeter with respect to the threshold level increase measurement uncertainty. A dynamic threshold which can adapt to varying particle and background video intensities will improve this condition. Such a technique is implemented in an edge-tracking routine described below that provides data for determination of particle shape and orientation.

D. Particle Shape and Orientation

Boundary definition using direction and curvature chains has been described by Eccles *et al.*[9] These techniques generally describe an image boundary in terms of a 1-D list of angles starting from an origin on the image edge and incrementing uniformly around the boundary. Freeman has described another method for determining shape by defining critical points around the boundary.[10] These points include discontinuities in curvature, points of inflection, curvature maxima, intersections, and points of tangency. Fourier transforms have been used as digital filters to smooth the digitized boundaries of planar objects. Pavlidis discusses several algorithms using Fourier transform coefficients to define detailed shape characteristics.[11] Teague has developed similar shape analysis techniques using Zernike moments.[12]

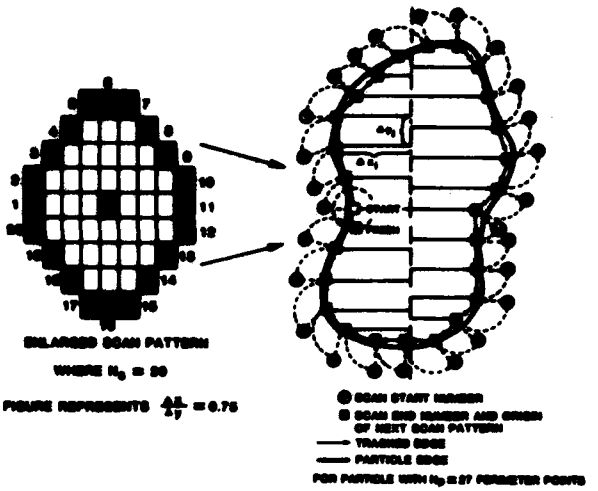

Fig. 4. Tracking algorithm.

We have chosen a boundary chain technique to determine particle shape and orientation which is similar to the method described by Eccles.[9] The edge-tracking algorithm, described below, determines the boundary between the particle and background by examining a small region of pixels along the particle edge. Edge detection is based on the intensity gradient between neighboring pixels rather than the simple threshold technique used in the particle scanning algorithm described above. As each new point along the particle edge is determined, the tracking pattern is then centered on that point and the new neighborhood is explored. This process continues until the particle has been fully circumnavigated. A more detailed discussion is given below.

E. Particle Edge-Tracking Technique

The particle edge-tracking algorithm provides the capability to classify particle size, shape, and orientation for applications dealing with particle settling dynamics. The edge-tracking algorithm scans across the particle edge in a series of small circular patterns where i is one of the N_p scans around the particle edge and j is one of the N_s points in a scan as shown in Fig. 4. The point j in the scan for which the pixel intensity $V(i,j)$ exceeds the previous pixel intensity $V(i,j-1)$ by a threshold value V_t is defined as the edge for the current scan pattern i and is used as the center of the next scan pattern $(i+1)$. This process continues until the scan returns to the neighborhood of the starting point. The scan radius R_s, number of points per scan N_s, and threshold value V_t, can be manually selected, depending on the particle size and shape.

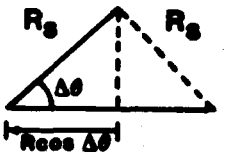

Fig. 5. Radial error due to $\Delta\theta$ affecting perimeter accuracy.

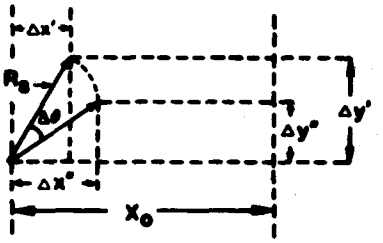

Fig. 6. Angular error affecting area accuracy.

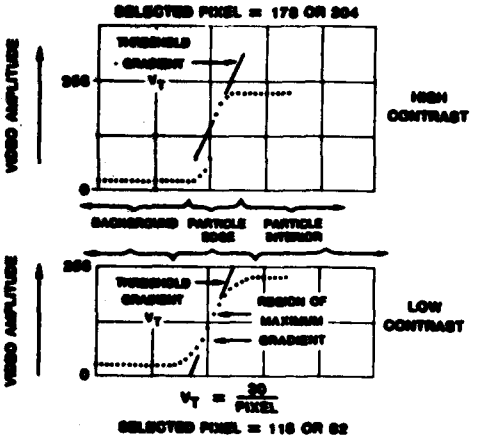

Fig. 7. Video amplitude across the edge of a high contrast (top) and low contrast (bottom) particle.

The perimeter of each particle is measured by accumulating the radial distance of each threshold transition around the particle edge until the circumnavigation of the particle is complete. Since the shape of each pixel is not square, both vertical and horizontal components must be scaled accordingly, by F_y and F_x, respectively, to provide an accurate measurement of the distance around the particle. The algorithm for this function is

$$\text{perimeter} = \sum_{i=1}^{N_p} [(F_y \cdot T_y)^2 + (F_x \cdot T_x)^2]^{1/2}, \tag{3}$$

where $T_y = R_s \sin$,
$T_x = R_s \cos$,
R_s = scan radius, and
N_p = number of threshold transition points along the edge.

The area of each particle is determined by accumulating the trapezoidal area defined by each new transition as shown in Fig. 4. The distance x_i between the particle edge and a vertical reference line at the center of the screen is determined for each transition point and multiplied by the vertical distance dy_i between two successive edges. The entire area of the particle is determined by successively adding or subtracting each incremental area depending on the vertical direction until the particle has been completely encircled as described by

$$\text{area} = \left(\frac{1}{2} \sum_{i=1}^{N_p} (x_i + x_{i+1}) \cdot dy_i \cdot F_y/F_x \right). \tag{4}$$

Particle identification from frame to frame is achieved by displaying the edge pixels of a selected particle on the next frame and comparing it with the shapes of the new particles for correlation.

F. Algorithm Error Analysis

The inherent error in the tracking process consists of radial and angular components, as shown in Figs. 5 and 6, respectively. These errors are functions of the number of scan points (N_s) and the scan radius (R_s), as shown in

$$\text{radial error} = R_s \cdot [1 - \cos(2\pi/N_s)]/2,$$
$$\text{Angular error} = +/-2\pi/N_s. \tag{5}$$

The error in determining the perimeter of a smooth boundary will produce a small positive error (e.g., 2.5% for $N_s = 20$) as shown in Eq. (6). However, the algorithm may exhibit a large negative error for figures with sharp corners because of truncation produced by the discrete scan process. The difference between the actual and measured area for large, smooth particles should be small but may become negative for particles with sharp corners, Eq. (7):

$$\text{perimeter error} = +N_p \cdot R_s(1 - \cos 2\pi/N_s), \tag{6}$$

$$\text{area error} = +/-(N_p \cdot R_s \cdot \sin 2\pi/N_2)/2. \tag{7}$$

Area and perimeter measurements will also vary as a function of the video intensity threshold value for the scan mode and as a function of the video intensity gradient threshold value for the tracking mode. The video amplitude across the edge of an image with varying contrasts is shown in Fig. 7. The effects due to variation of the threshold values on measurements of a high-contrast, white-on-black square (2 cm/side) are summarized in Table II. In generating these data the video threshold intensity for the scan mode was set at values from 23% to 74% of the intensity difference between the square and the background, whereas the intensity gradient threshold (intensity difference/pixel) for the tracking algorithm was varied from 8% to 32% of the total intensity difference between the square and the

Table II. Effects of Variation of Video Threshold Intensity (Scan) and Intensity Gradient (Track); Variation is Represented by ±1 Standard Deviation as well as the Total Range of Deviation

Area (pixels)		Perimeter (pixels)	
Scan	Track	Scan	Track
2168.6 ± 4.0% 11% Range	2068.1 ± 1.3% 4% Range	186.6 ± 4.7 18% Range	189.4 ± 1.7% 5.9% Range

Fig. 8. Photograph of video image of hologram of mica flake. The video amplitude of each pixel along the central white line is shown by the relative scale on the right-hand side of the screen. The length and width of this particle were 41 and 19 μm, respectively.

background. A negative threshold gradient (i.e., a bright-to-dark transition) was used to determine the edge in this particular application.

The range of threshold effects is smaller for the tracking mode than the scanning mode because the maximum video intensity gradient, generally found about halfway between the intensities of the image and the background (see Fig. 7), cannot be exceeded without the algorithm losing track of the particle edge. The threshold intensity gradient value for the tracking program is generally selected to be smaller than the smallest normal edge gradient (bottom curve in Fig. 7) found along the particle edge. This insures that oblique approaches to the edge do not reduce the measured intensity gradient below that of the threshold. This reduced threshold value causes the tracking program for the high-contrast part of the particle (upper curve, Fig. 7) to, in effect, underestimate the size of the particle for a white-on-black image and overestimate the size of a particle for a black-on-white image, especially for particles of varying contrast along the edges. For the white square on black background image addressed in Table II, this resulted in particle size estimates that were ½ to 1½ pixels lower per edge transition (see upper curve in Fig. 7), depending on the video threshold intensity gradient selected or a 1.2 to 3.6% underestimate of the length of each side. This underestimate would be offset to some extent by the radial error effect on the perimeter as described by Eq. (6).

V. Performance Evaluation

The performance of the scan and track algorithms was evaluated using white-on-black geometrical figures (square, equilateral triangle, and circle) of controlled size and shape. The figures are typical in projected size onto the TV screen of magnified holograms of 50–150-μm particles. They do not push the limits of resolution of the system since our primary objective was to test the performance of various image analysis algorithms as a function target size and shape. The standards for comparison were accurate to within ½ to 1 pixel/side or to about ±2.5% for the small figures and ±1.25% for the large. The results of the comparisons are shown in Table III. Digitization error appears to have produced a greater effect on accuracy of the small figures with complex shapes compared with the larger ones. A digitization error of 1 pixel/edge can result in errors as large as ±3.6% for the small and ±2.0% for the large triangle measurements. However, this effect should approach zero as the shapes become larger and smoother.

For the tracking program, most errors did not exceed the accuracy limits of the standard measurement. Digitization errors, together with the uncertainties in the standards, can account for the differences between the measured and standard sizes; inclusion of the potential of radial, corner-truncation, and threshold intensity/threshold intensity gradient errors insures that the maximum tracking error measured (3.98%) falls within potential error limits.

For the scan program, all the areas measured were within expected error limits, although the triangle and circle perimeter errors were larger. The perimeter errors for the squares were quite low as the edges of each square were aligned with the vertical and horizontal axes of the TV camera. Perimeters in the scan mode can be exaggerated by as much as $1 - \sqrt{2}/2$ for lines sloping 45° to the vertical. The largest manifestation of this serrated-edge effect was found for the circle, with more than a +14% error.

VI. Application to Holograms

The application of these techniques was demonstrated by reexamining *in situ* transmission holograms of mica flakes collected during the settling experiment reported in Ref. 5. Because the mica flakes are very thin and tend to settle at some angle to the focal plane, only one side can be in sharp focus at any time. Therefore, a slightly defocused (lower contrast) image was analyzed (Fig. 8). This lower contrast image is

Table III. Perimeter and Area Measurement Accuracies of the Scanning and Tracking Algorithms for Some Standard Geometrical Shapes

Shape	Size (cm)	Track Area % Error	Track Perimeter % Error	Scan Area % Error	Scan Perimeter % Error
Square	3.0	0.36	−0.47	0.50	+1.4
Square	2.0	0.96	0.17	+2.89	+3.2
Triangle	4.0	−3.00	−2.90	−0.56	6.89
Triangle	2.2	+3.96	+1.83	−0.80	+4.23
Circle	4.0	−0.90	0.62	+3.14	+14.45
Circle	2.2	−0.66	2.97	+0.66	+9.76

Table IV. Holographic Image Analysis Measurements of Falling Mica Plates Using the Scanning and Tracking Algorithms (Pixels)

Sample	Scanning Area	Scanning Perimeter	Scanning Threshold	Tracking Area	Tracking Perimeter	Tracking Threshold gradient	General shape	Longest dimension (μm)
1	496	127	134	500	135	26	Elliptical	41
2	107	40	113	101	42	30	Elliptical	14
3	485	118	100	501	106	30	Elliptical	42

typical of the type collected from irregularly shaped particles commonly found in seawater.

A comparison between the tracking and scanning algorithm data (Table IV) shows that the areas generated are within ~6% of each other for these mica holograms. However, the elliptical image of the third measurement resulted in a perimeter that was 11% higher for the scanning than for the tracking algorithm. The long axis of this image was diagonal to the screen axes, and the scanning algorithm overestimated the perimeter by serrating the diagonally oriented edges.

VII. Summary

The holographic microvelocimeter has proven to be an invaluable tool in studying the settling dynamics of particles in both marine and laboratory environments. The reduction of data from this instrument has been semiautomated using a microcomputer to control two phases of the analysis and provide data storage and retrieval. During the first phase of the analysis a precision translation stage is controlled to bring a sequence of holographic frames into register for the 3-D measurement of particle displacement between frames. Control of this stage is of the order of ±0.0002 cm with even greater accuracies in particle settling velocities being achieved by increasing the hologram exposure interval.

The second phase of the analysis is the measurement of the size, shape, and perimeter of the digitized video image of suspended particles within the hologram. Two techniques have been developed to measure the area and perimeter of an image. Both methods have been tested with standard geometric as well as holographic images and are accurate to within 4–6%. The first method utilizes a scanning algorithm based on absolute video intensity for edge detection. Although the algorithm is quite fast and is able to scan the area and perimeter of a particle in a single pass, accuracy is compromised for very noisy low-contrast particles or for particles with long diagonal edges. The second method uses a tracking algorithm based on video intensity gradient for edge detection. This technique not only provides accurate area and perimeter measurements but also produces detailed edge coordinates which can be used for complex shape identification. Although this system has been applied to the study of particle settling dynamics, the techniques developed could also be applied to other pattern recognition and image analysis problems.

This effort was funded under Office of Naval Research contract N00014-75-C-0539 to the Marine Science Department, University of South Florida.

References

1. R. A. Briones, L. O. Heflinger, and R. F. Wuerker, Appl. Opt. 17, 944 (1978).
2. L. O. Heflinger, G. L. Stewart, and C. R. Booth, Appl. Opt. 17, 951 (1978).
3. K. L. Carder, Opt. Eng. 18, 524 (1979).
4. K. L. Carder and D. J. Meyers, Proc. Soc. Photo-Opt. Instrum. Engr. 208, 151 (1979).
5. L. J. Doyle, K. L. Carder, and R. G. Steward, J. Sediment. Petrol. 53, 2 (1983).
6. K. L. Carder, R. G. Steward, and P. R. Betzer, J. Geophys. Res. 87, 5681 (1982).
7. Y. Yakimovsky, Fourth International Joint Conference on Artificial Intelligence (1974).
8. J. W. McKee and J. K. Aggarwal, Pattern Recognition 7, 25 (1975).
9. M. J. Eccles, M. P. C. McQueen, and D. Rosen, Pattern Recognition 9, 31 (1977).
10. H. Freeman, Pattern Recognition 10, 159 (1978).
11. T. Pavlidis, IEEE Trans. Pattern Anal. Machine Intell. PAMI-2, 301 (1980).
12. M. R. Teague, J. Opt. Soc. Am. 70, 920 (1980).

THE HYDRAULIC EQUIVALENCE OF MICA[1]

LARRY J. DOYLE, KENDALL L. CARDER, AND ROBERT G. STEWARD
Department of Marine Science
University of South Florida
104 Seventh Avenue South
St. Petersburg, Florida 33701

ABSTRACT: Settling experiments performed on silt- to fine-sand-sized mica flakes with a holographic micro-velocimeter revealed that mica is the hydraulic equivalent of quartz spheres having diameters a factor of 4 to 12 times smaller. Mica in the very fine to fine-sand sizes has been traditionally used by sedimentologists to delineate areas of deposition or nondeposition and potential winnowing of fines, and is here found to be the hydraulic equivalent of silt-sized particles but not of clay.

Experiments also showed that mica flakes tend to settle at orientations which are neither perpendicular nor parallel to the gravitational vector and tend to generally maintain their orientation throughout. Equations for the settling of a disc in Lerman and others (1974) and that developed by Komar and Reimers (1978) are shown to be mathematically similar for the coarse-silt to fine-sand ranges of discs and are adequate predictors of settling rates of mica flakes. A comparison of the hydraulic equivalency of quartz spheres to coarse-silt- through fine-sand-sized mica flakes is presented.

INTRODUCTION

Because it cleaves into flaky particles, sand-sized mica is a mineral group in which shape should obviously affect settling charateristics and, in fact, has often been considered to be the hydraulic equivalent of silt and clay. Neihesel (1965) noted the *close association* between sand-sized mica and the clay fraction of Georgia estuaries, an association also recognized by Pamerancblum (1966) off Israel. Doyle and others (1968) used the abundance of mica in the 125- to 250-μm size fraction to delineate areas of the southeastern United States continental margin that might be undergoing winnowing or deposition of fines, a process which otherwise would be masked by the dominance of reworked Pleistocene sands. A similar approach was used by Adegobe and Stanley (1972) on the Niger Shelf. Doyle and others (1979) and Park and Pilkey (1981) discuss the significance of mica content to the depositional and erosional systems of the whole continental margin of the Eastern United States.

Despite its intuitive widespread use as a hydraulic analog of finer sized sediments, no quantitative evaluation of the sedimentologic characteristics of mica has yet been undertaken. The purpose of this paper is to determine as far as possible the hydraulic characteristics of mica flakes and how these characteristics compare with those predicted from settling equations in the literature.

APPROACH

Our approach is to utilize a modified holographic micro-velocimeter developed and described by Carder (1978) and Carder and Meyers (1979). Figure 1 shows the system used. Transmission holograms are simultaneously collected along the vertical and horizontal axes of a settling cuvette. A reference point in the cuvette is also recorded on each vertical and horizontal hologram to allow translation between the two axes. Sequential frames at accurately timed intervals (from 0.5 to 3.0 seconds depending on the particle size) record the settling velocity and orientation as well as particle size and shape. The images are reconstructed by placing the hologram back into the laser path and refocusing on particles in any of the infinite number of focal planes in the settling cuvette. This system offers the advantage of using actual sedimentary particles in the sand- to clay-size ranges, thus obviating any errors that may be inherent in scale modeling systems.

Mica samples were chosen from sediment cores from the Eastern United States continental slope (Doyle and others, 1979). Silt- to fine-sand-sized mica flakes were added to a small

[1]Manuscript received February 26, 1982; revised September 29, 1982.

 0022-4472/83/0053-0643/$03.00

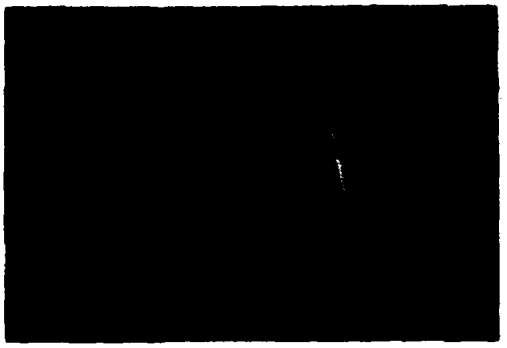

FIG. 1.—Holographic micro-velocimeter setup used to measure the settling velocity of the mica flakes.

quantity of filtered distilled water to obtain a slurry. A drop of slurry was picked up on a fine brush and the drop barely touched to the top of the miniscus of the distilled filtered water in the cuvette, thereby introducing mica flakes into the measuring apparatus. Other methods of sample introduction, including use of an eye dropper, were tried, but they tended to set up convection within the cuvette.

Resulting settling velocities were then compared with the theoretical settling rates generated from the equations of Lerman and others (1974) and Komar and Reimers (1978). In the calculations of settling rates a density for mica of 2.9 g/cm^3 was used, midway in the normal range for biotite and muscovite. Examination of the mica by standard optical techniques showed that the mica fraction in the cores was composed of muscovite and a lesser amount of biotite. Finally, we compared the measured settling rates of the mica with those for quartz spheres.

SHAPES AS A FACTOR OF GRAIN SETTLING

Shape has been recognized as an important factor in the analysis of sediments by hydraulic methods (principally settling tube) for over 100 years. Gibbs and others (1971), Lerman and others (1974), Komar and Reimers (1978), and Brezina (1979) have summarized the development of thinking concerning the hydraulic importance of shape and have contributed to the formulation of equations for settling velocity that take grain shape into account. In a series of recent articles Baba and Komar (1981a and b) have begun to examine shape effects of various types of natural particles.

Lerman and others (1974) modified the equations for the settling of a disc of "no thickness" in the Stoke's range, developed by Lamb (1932), Payne and Pell (1960), and Brenner (1964), by adding a term for disc thickness. The resulting formulae for the two major orientations of fall are:

$$U = \frac{g(\rho_s - \rho)\, q_h r^2}{3.396\, \mu} \text{ (edgewise)} \qquad (1)$$

$$U = \frac{g(\rho_s - \rho)\, q_h r^2}{5.1\, \mu} \text{ (broadside)}, \qquad (2)$$

where U = settling speed; r = disc radius; h = thickness; q_h = h/r; μ = dynamic viscosity of water; ρ_s = particle density; ρ = density of water; and g = acceleration due to gravity (981 cm/sec^2).

Komar and Reimers (1978) approached the effect of shape on settling velocity by scale modeling with pebbles in a glycerine settling medium, the results being equivalent to quartz sand and silt in water. They found experimentally that the Corey Shape Factor (CSF) introduced by Corey (1949), Malaika (1949), McNown and Malaika (1950), and McNown and others (1951) gave the best prediction of shape effects for the pebbles they used in their experiment. Based upon their experimental results, Komar and Reimers (1978) developed an empirical formula for settling velocity in the Stoke's range, taking into account shape effect:

$$U = \frac{1}{18\, \mu}\, \frac{1}{f(CFS)}\, (\rho_s - \rho)\, g D_n^2, \qquad (3)$$

where $D_n = (hD_iD_l)^{1/3}$; D_i = intermediate axis particle diameter; D_l = principal axis particle diameter; CSF = $h/\sqrt{D_iD_l}$; h = small axis particle diameter; $f(CSF) = 0.946(CSF)^{-0.378}$ when $0.4 \leq CSF \leq 0.8$; and $f(CSF) = 2.18 - 2.09\,(CSF)$ when $CSF \leq 0.4$.

They further found that they could extend the range of the grain sizes following Stoke's settling to Reynolds numbers of up to 0.10 or for particles of up to 100 μm, and they were able to empirically extend their data to cover grain sizes up through pebbles. For particles like mica where h is small relative to D_i and D_l, CSF is ≤0.4 and the general equation (3) becomes:

$$U = (1/18\,\mu)\frac{1}{[2.18 - 2.09\,(h/\sqrt{D_1D_1})]} \cdot(\rho_s - \rho)\,g(hD_1D_1)^{2/3} \quad (4)$$

The particle thickness h may be expressed as a ratio with respect to D, that is, D/100, D/50, D/25 . . . D/χ, and therefore in the ranges in which we are working, the equations of Lerman and others (1974) and equation (3) are similar. For example, let $D_1 = D_1 = \bar{D}$, $\chi = \bar{D}/h = 2r/h$, and $q_h = h/r$. Then equation (4) becomes:

$$U = \frac{1}{18\mu}\frac{1}{\left(2.18 - 2.09\,\frac{1}{\chi}\right)} \cdot(\rho_s - \rho)g\left(\frac{\bar{D}^3}{\chi}\right)^{2/3}$$

$$U = \frac{1}{\left(2.18 - 2.09\,\frac{1}{\chi}\right)\chi^{2/3}} \cdot\underbrace{\frac{1}{18\mu}(\rho_s - \rho)\,g\bar{D}^2}_{\text{Stoke's Formula}}. \quad (5)$$

Our measurements of h for mica flakes yielded a range of $h \simeq 0.007D - 0.05\,D$. For $\chi = \bar{D}/h = 1/0.01 = 100$, and substituting in (5), we obtain:

$$U = 0.021\,\frac{1}{18\mu}(\rho_s - \rho)\,g\bar{D}^2.$$

Lerman's formulae are of the general form

$$U = \frac{g(\rho_s - \rho)\,q_h r^2}{c\mu},$$

where c = 3.396 to 5.1. Substituting as before we obtain

$$U = \frac{g(\rho_s - \rho)\,D^2}{2c\mu\chi}.$$

Multiplying by 18/18 yields

$$U = \frac{18}{2c\chi}\underbrace{\frac{1}{18\mu}(\rho_s - \rho)\,gD^2}_{\text{Stoke's Formula}}.$$

For Lerman's formula to be equivalent to Komar and Reimers at $\chi = 100$ we can set

$$\frac{18}{2c\chi} = 0.021$$

$$c = \frac{18}{2(100)(0.021)}$$

$$c = 4.28.$$

This value lies between Lerman's two values of 3.396 and 5.1, and therefore values derived from the two sets of formulae will be close to each other over the ranges we are examining.

Assuming $D_i = D_1 = \bar{D}$ (where $\bar{D}$ is an average diameter) is an idealized case which all mica flakes do not meet. Any deviation from $D_i = D_1$ will obviously cause some deviation in the calculation of μ. When $D_i = D_1$, the parameter $\chi = D/h$ becomes the shape parameter directly related to the Corey shape factor.

THE HYDRAULIC EQUIVALENCY OF MICA

In our experiments mica flakes seldom settled either exactly broadside or edgewise. They usually assumed an orientation between the two extremes, neither perpendicular nor parallel to the gravitational vector which they maintained throughout. Stringham et al. (1969) also showed that particles settling at low Reynolds numbers maintain their initial orientation which need not be perpendicular to the settling direction.

Figure 2 shows the experimentally determined settling velocities of mica flakes plotted on the family of curves of Lerman and others (1974) and Komar and Reimers (1978) for thicknesses of D/200, D/50, D/20, and D/10. Komar and Reimer's (1978) equation begins to diverge from those of Lerman (1974) only at thicknesses of D/20 and greater. The thicknesss/D ratios of 32 mica grains from a split of the slope sediment used for the settling velocity experiment were determined by scattering some quartz beach sand on an SEM stub and then sprinkling the mica-rich slope sample over it. Some of the mica flakes landed on edge and we were thus able to measure thickness-to-D ratios. Thicknesses ranged from 0.7 percent of D to 5 percent of D, with the average at 2 percent and a standard deviation of 1.15 percent. Figure 2 also shows that most of the velocities of mica flakes that we measured fall within the envelope created by the theoretical curves. Scatter at the courser end is probably mostly the result of variation in thickness,

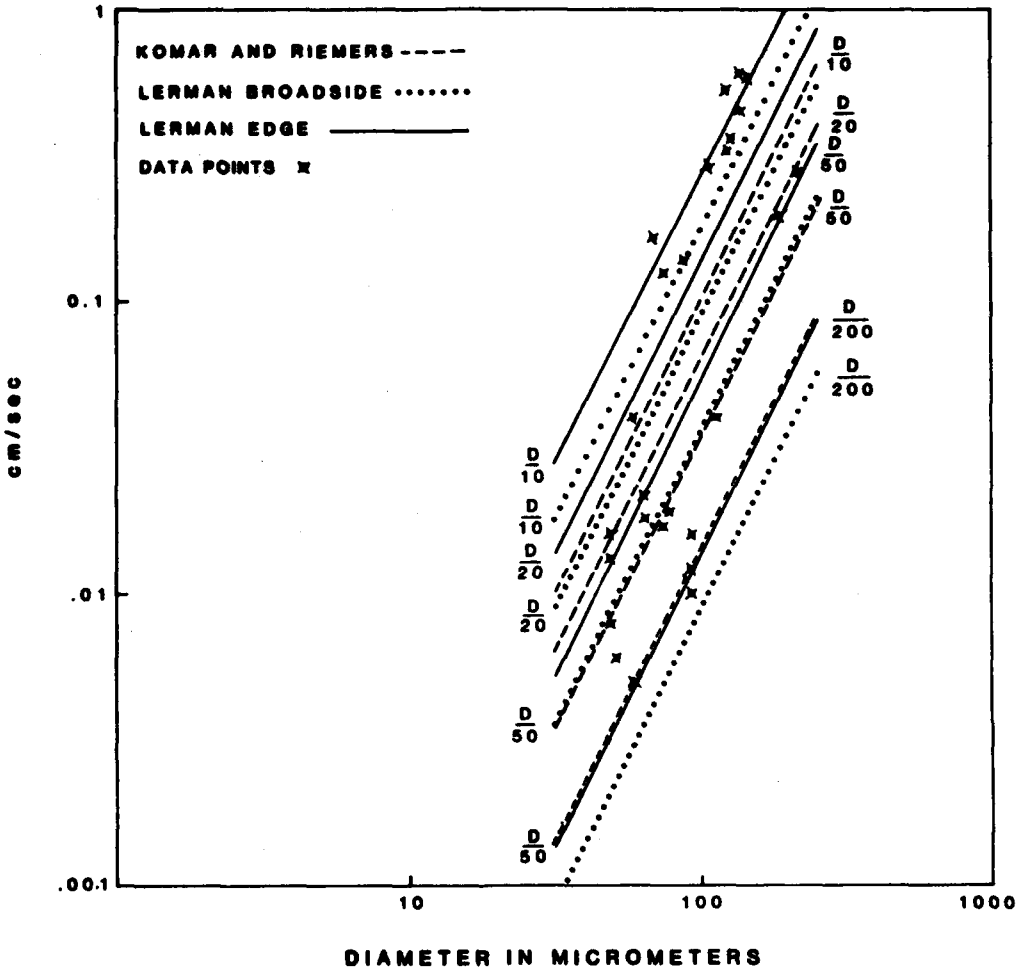

FIG. 2.—Lerman and others (1974) equations for the settling of discs both broadside and edgewise plotted along with that of Komar and Reimers (1978) for thickness of D/200, D/50, D/20, and D/10. Note that the equations yield values which are very close to each other at thicknesses of D/50 or less, thicknesses most prevalent for mica flakes. X's are values of mica flakes we measured.

symmetry (for example, $D_l \neq D_l$) and settling orientation, because some particles in this size range are beginning to exceed the Stoke's low Reynolds number constraint on the Stoke's equation.

At the coarser end of the scale, particles fall closer to the equations of Lerman and others (1974) than to that of Komar and Reimers (1978). Figure 3 shows the diameter of spherical quartz particles of density of 2.65 which would settle at rates of the variously sized mica flakes determined from the equations of Lerman and others (1974) for h = D/200, D/50, and D/20. Our experiments show that mica ranging in diameter from 62 μm to 250μm, with a thickness of no more than 5 percent of the sieve diameter, is the hydraulic equivalent of 5-μm to 82-μm quartz spheres. Very fine, sand-sized mica, then, is the hydraulic equivalent of silt-sized quartz spheres whereas fine-sand-sized mica is the equivalent of silt- to very fine sand-sized spheres. Coarse-silt-sized mica flakes are the equivalent of fine, and very fine quartz silts.

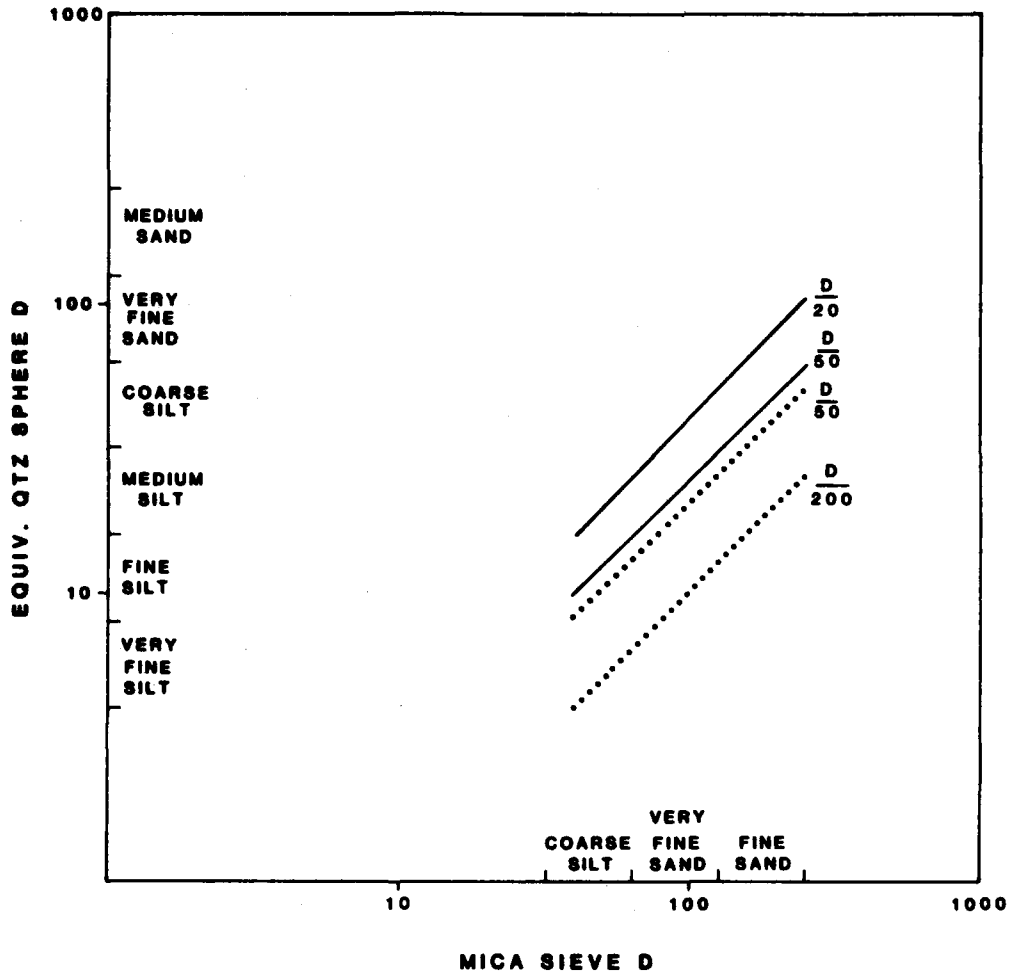

FIG. 3.—The hydraulic equivalency of mica to quartz spheres. Mica sizes are coarse slit to fine sand, and thicknesses are D/200, D/50, and D/20.

CONCLUSIONS

1) The equations for determining settling velocity of a disc presented by Lerman and others (1974) and that developed by Komar and Reimers (1978) for particles where the Corey Shape Factor ≤ 0.4 are similar for thicknesses of D/50 or less.

2) Experiments on fine-sand- to coarse-silt-sized mica flakes using a holographic micro-velocimeter showed that grains most often do *not* orient themselves perpendicular to the flow field as they settle but that they tend to settle at some orientation between broadside and edgewise.

3) Mica in the coarse-silt, very fine sand, and fine-sand sizes is the hydraulic equivalent of silt- and very fine sand-sized quartz spheres according to the relationships shown in Figures 2 and 3.

Contrary to previous assumptions, mica in the coarse-silt to fine-sand sizes is not the hydraulic equivalent of clay.

ACKNOWLEDGMENTS

This research was partially supported under Office of Naval Research Contract No. N00014-75-C-0539. Gregg Brooks and Robert Byrne

critically reviewed some of the manuscript. The authors wish to acknowledge the especially thorough review of Paul Komar who pointed out a more elegant comparison between the equation of Komar and Reimers and the equations of Lerman than we had originally presented and which we have incorporated into this paper.

REFERENCES

ADEGOBE, O. S., AND STANLEY, D. J., 1972, Mica and shell as indicators of energy level and depositional regime on the Nigerian shelf: Marine Geology, v. 13, p. M61–66.

BABA, J., AND KOMAR, P. D., 1981, Settling velocities of irregular grains at low Reynolds numbers: Jour. Sed Petrology, v. 51, p. 121–128.

BABA, J., AND KOMAR, P. D., 1981, Measurements and analysis of settling velocities of natural quartz sand grains: Jour. Sed. Petrology, v. 51, p. 631–640.

BRENNER, H., 1964, The Stoke's resistance of a slightly deformed sphere: Chem. Eng. Sci. 19, p. 519–539.

BREZINA, J. 1979, Particle size and settling rate distributions of sand-sized materials: Second European Symposium on Particle Characterization, Nuremberg, September 24–26, 1979, 44 p.

CARDER, K. L., 1978, A holographic micro-velocimeter for use in studying ocean particle dynamics: SPIE Vol. 160 Ocean Optics V, p. 63–66.

CARDER, K. L., AND MEYERS, D. J., 1979, New optical techniques for particle studies in the bottom boundary layer: SPIE vol. 208 Ocean Optics VI, p. 151–158.

COREY, A. T., 1949, Influence of shape on the fall velocity of sand grains. [unpub. Masters thesis]: Colorado A&M College, 102 p.

DOYLE, L. J., CLEARY, W. J., AND PILKEY, O. H., 1968, Mica: its use in determining shelf-depositional regimes: Marine Geology, v. 6, p. 381–389.

DOYLE, L. J., PILKEY, O. H., AND WOO, C. C., 1979 Sedimentation on the Eastern United States continental slope, *in* Doyle, L. J., and Pilkey O. H., eds., Geology of Continental Slopes: Soc. Econ. Paleontologists Mineralogists Spec. Pub. no. 27, p. 119–129.

GIBBS, R. J., MATTHEWS, M. D., AND LINK, D. A., 1971, The relationship between sphere size and settling velocity: Jour. Sed. Petrology, v. 41, p. 7–18.

KOMAR, P. D., AND REIMERS, C. E., 1978, Grain shape effects on settling rates: Jour. Geology, v. 86, p. 193–209.

LAMB, H., 1932 (1945), Hydrodynamics (Sixth edition): New York, Dover.

LERMAN, A., LAL, D., AND DACEY, M. F., 1974, Stoke's settling and chemical reactivity of suspended particles in natural waters, *in* Gibbs, R. J., ed., Suspended Solids in water: New York, Plenum Press, p. 17–47.

MALAIKA, J., 1949, Effect of shape of particles on their settling velocity, [unpub. Ph.D. dissertation]: State Univ. Iowa. 64 p.

MCNOWN, J. S., and MALAIKA, J., 1950, Effects of particle shape on settling velocity at low Reynolds numbers: Trans. American Geophysical Union, v. 31, p. M74–82.

MCNOWN, J. S., MALAIKA, J., AND PRAMANIK, H., 1951, Particle shape and settling velocity: Proc. Intern. Assoc. Hydr. Res., fourth meeting, Bombay, India, p. 511–522.

NEIHEISEL, J., 1965, Source and distribution of sediments at Brunswick Harbor and vicinity Georgia: U. S. Army Coastal Engineering Res. Center Tech. Memo. 12, 21 p.

PAMERANCBLUM, M., 1966, The distribution of heavy minerals and their hydraulic equivalents in sediments of the Mediterranean continental shelf off Israel: Jour. Sed. Petrology, v. 36, p. 162–174.

PAYNE, L. E., and PELL, W. H., 1960, The Stokes' flow problem for a class of axially symmetric bodies: Jour. Fluid Mech., v. 7, p. 529–549.

PARK, Y. A., AND PILKEY, O. H., 1981, Detrital mica: environmental significance of roundness and grain surface textures: Jour. Sed. Petrology, v. 51, p. 113–120.

STRINGHAM, G. E., SIMONS, D. B., GUY, H. P., 1969, The behavior of large particles falling in quiescent liquids: U.S. Geological Survey Prof. Paper 562-C, 36 p.